Investigation of interface properties of sputter deposited TiN/CrN superlattices by low-angle X-ray reflectivity

Harish C. Barshilia[a)], N. Selvakumar and K. S. Rajam
Surface Engineering Division, National Aerospace Laboratories
Post Bag No. 1779, Bangalore – 560 017, India

K. Gopinadhan and Sujeet Chaudhary
Department of Physics, Indian Institute of Technology, Delhi - 110 016, India

Abstract

Approximately 1.8 μm thick nanolayered multilayer coatings of TiN/CrN (also known as superlattices) were deposited on silicon (100) substrates at different modulation wavelengths (4.6–12.8 nm), substrate temperatures (50-400 °C) and substrate bias voltages (-50 to -200 V) using a reactive direct current magnetron sputtering system. X-ray reflectivity (XRR) technique was employed to determine various properties of the multilayers such as interface roughness, surface roughness, electron density, critical angle and individual layer thicknesses. The modulation wavelengths of the TiN/CrN superlattice coatings were calculated using modified Bragg's law. Furthermore, the experimental X-ray reflectivity patterns were simulated using theoretically generated patterns and a good fit was obtained for a three layer model, i.e., (1) top surface roughness layer, (2) TiN/CrN multilayer coating (approximately 1.8 μm) and (3) Ti interlayer (~ 0.5 μm) at the film-substrate interface. For the superlattice coatings prepared at a modulation wavelength of 9.7 nm, a substrate bias of -200 V and a substrate temperature of 400 °C the XRR patterns showed Bragg reflections up to 5th order, indicating well-defined

[a)]Author to whom correspondence should be addressed
Electronic mail: harish@css.nal.res.in
Fax # +091-80-2521 0113

periodicity of the constituent layers and relatively sharp interfaces. The simulation showed that the superlattice coatings prepared under the above conditions exhibited low surface and interface roughnesses. We also present the effect of substrate temperature and substrate bias, which are critical parameters for controlling the superlattice properties, onto the various interface properties of TiN/CrN superlattices.

1. Introduction

Nanolayered multilayer coatings, also known as superlattices, consist of alternating layers of two different materials with a modulation wavelength or bilayer thickness (Λ) in the range of nanometers. In recent years, various nanolayered multilayer coatings such as TiN/CrN, TiN/NbN, TiAlN/TiN, TiAlN/CrN, etc. have been extensively studied due to their improved properties compared to single layer coatings [1-7]. Transition metal nitride superlattices exhibit superior mechanical and tribological properties and also exhibit superior oxidation resistance [1-3, 7-9]. These coatings can be used for cutting, punching, forming, injection molding, drilling, milling and tribological applications [10]. The structure, mechanical, tribological properties, and oxidation and corrosion resistance of TiN/CrN nanolayered multilayered coatings have been studied in great detail in the literature [2,9,11-17]. The unique combination of high fracture resistance and high abrasion resistance of TiN/CrN multilayers make this coating an interesting choice for a number of tool applications where high tensile stresses are generated in the coating [2].

Superlattices with periodic structures are characterized, based on two structural parameters: (1) the modulation wavelength and (2) the thickness distribution between the two components [18]. The modulation wavelength plays an important role in determining the properties of the multilayer coatings. The thickness distribution leads to accumulation of

interface roughness, resulting in deterioration of properties of the multilayer coatings [19]. The multilayer coatings exhibit superior properties only at very low modulation wavelengths. Therefore, determination of the modulation wavelength is very important. Conventionally, cross-sectional transmission electron microscopy (XTEM) has been used to determine the modulation wavelength of the multilayers [20]. But XTEM is a destructive technique and the sample preparation is tedious and challenging. Alternative method such as low angle X-ray reflectivity (XRR) has been used to determine the modulation wavelength of the multilayer coatings [21-27]. X-ray reflectivity is non-destructive and more reliable than XTEM and provides information about the average features of the sample over all the macroscopically studied area.

Low angle X-ray reflectivity is a non-destructive technique widely used to determine individual layer thicknesses, electron densities (ρ_e), critical angle (θ_c), interface (σ) and surface roughnesses (σ_0) of multilayered coatings deposited on flat substrates. The reflectivity in a multilayer depends on the difference in the electron densities between the two layers [21]. While passing from air (n = 1) to the material (n < 1) it is possible to reflect the beam if the incident angle θ_m (which is the angle between the surface of the sample and incident beam) is small enough. This is known as the total external reflection of X-rays and the angle is called as critical angle. For small angle of incidence and neglecting absorption, the value of θ_c expressed in radians, is related to θ_m and individual layer thickness, by [28]:

$$\theta_c^{\,2} = \theta_m^{\,2} - \left(\frac{\lambda}{2t_{per}} \right)^2 m^2 , \tag{1}$$

$$t_{per} = t_A + t_B , \tag{2}$$

where, t_A and t_B are the thicknesses of the two individual layers A and B.

At a certain incident angle θ_m, path difference is equal to multiple of X-ray wavelength (λ), and the constructive condition for X-ray diffraction is satisfied to generate a reflection peak [22]:

$$m\lambda = 2\Lambda \sin\theta_m \left(1 - \frac{4\bar{\delta}\Lambda^2}{m^2\lambda^2}\right), \quad (3)$$

where m is the order of the reflection, Λ is the modulation wavelength and $\bar{\delta}$ is a density average profile value for a bilayer pair.

By combining the Snell's and the Bragg's laws and through mathematical approximation, the modified Bragg's law can also be expressed as [23,24,29]:

$$\sin^2\theta_m = (m\lambda/2\Lambda)^2 + 2\delta. \quad (4)$$

According to Eq. (4) a linear fit to the observed data can be made by plotting $(m\lambda)^2$ versus $\sin^2\theta_m$. The slope of the resulting line is then equal to $4\Lambda^2$, and from this Λ can be derived.

Detailed studies on the interface properties of various magnetic multilayers (e.g., Co/Re, Co/Cu) [30,31] and multilayer X-ray mirrors (e.g., Nb/Si, Cr/Sc, Mo/Si) have been reported in the literature [27,32,33]. To our knowledge, detailed studies on sputter deposited transition metal nitride superlattices using low angle X-ray reflectivity have not been reported so far [8,34]. In this paper, TiN/CrN superlattices were deposited using a reactive direct current (DC) magnetron sputtering technique. We study the effect of three most important parameters: modulation wavelength, substrate bias (V_B) and substrate temperature (T_S), on the various properties of the coatings (such as critical angle, electron density, interface and surface roughness). These parameters control mechanical properties of transition metal nitride superlattices. The structure and mechanical properties of these coatings are described in detail

elsewhere [3]. Here we present the results of experimental and simulated low angle X-ray reflectivity measurements.

2. Experimental details

Alternate layers of TiN and CrN of varying thicknesses were deposited on silicon (100) substrates using a reactive DC magnetron sputtering system that has been described elsewhere [3]. The root mean square roughness of the substrates, as measured by the atomic force microscopy, was approximately 0.75 nm. In order to get varying thicknesses of TiN and CrN layers, 0.075 m diameter high purity Ti (99.95%) and Cr (99.99%) targets were sputtered for different durations in high purity argon (99.999%) and nitrogen (99.999%) plasma. The power densities were 5 and 2 W/cm^2 for Ti and Cr targets, respectively. Typically, TiN/CrN multilayers were deposited under a base pressure of 5.0×10^{-4} Pa and a total $Ar+N_2$ gas pressure of 5.0×10^{-1} Pa. The operating pressure, which controls the quality of the sputtered coating, was kept constant for all the samples. A total nitrogen flow rate of 2.0 sccm was used for all the depositions. The sputtering guns were shielded from each other so that no overlap of the two particle beams occurred. It is known that CrN exists in different phases (c-CrN and β-Cr_2N) and there is a limited range of nitrogen concentration wherein stoichiometric phases of TiN and CrN with B1 NaCl structure exist. The deposition conditions were, therefore, carefully optimized after a series of experiments involving variations of nitrogen partial pressure, target power, operating pressure and substrate bias [3]. Different partial pressures of nitrogen were maintained in the deposition chamber to deposit nearly stoichiometric TiN and CrN coatings as the heat of formation of CrN (29.8 kcal/mol) is considerably less than that of TiN (80.8 kcal/mol) [35]. Furthermore, the nitrogen partial pressures were carefully chosen as the homogeneity range of c-CrN is very narrow, extending from 49.5 to 50.0 at.%, whereas, for TiN it is from 38.0 to 50.0

at.% [36]. The nitrogen gas was introduced through a manifold in front of the chromium target in order to maximize the nitridation of depositing chromium and minimize that of depositing titanium, thus ensuring a higher partial pressure of nitrogen near the chromium target.

Three sets of TiN/CrN superlattices were prepared. In the first set, the TiN/CrN superlattices were deposited at different nominal modulation wavelengths ranging from 4.0 – 12.0 nm. The experimental conditions for these coatings are shown in Table 1. The nominal modulation wavelength was calculated from the growth rates of TiN (0.2 nm/s) and CrN layers (0.6 nm/s)), wherein the growth rates were calculated from the thicknesses of the coatings examined under cross-sectional scanning electron microscope. In the second set, the substrate bias voltage was varied from -50 to -200 V, keeping the substrate temperature (T_S = 400ºC), the nominal modulation wavelength (9.0 nm) and the number of bilayers (238) constant. The third set was deposited at different substrate temperatures in the range 50–400ºC with a nominal modulation wavelength of 9.0 nm, a substrate bias of -200 V and total bilayers of 238. The substrates were chemically cleaned in an ultrasonic agitator in acetone, absolute alcohol and trichloroethylene. Subsequently, the substrates were cleaned in situ by Ar^+ ion bombardment for 30 min, wherein a DC bias of -850 V was applied to the substrate at an argon pressure of 6.0×10^{-1} Pa. A 0.5 μm thick Ti interlayer was deposited for all the samples to improve the adhesion of the coatings. Under these conditions, typical growth rates were 0.2 and 0.6 nm/s for TiN and CrN, respectively. In order to deposit multilayer coatings with controlled layer thicknesses and repeatability, a PC based control system was used. This system consisted of a driver circuit power supply and a stepper motor connected to the substrate holder through a rotary feedthrough. The driver circuit was controlled by a computer. The total thicknesses of the

coatings were approximately 1.8 μm. The first layer on the substrate was always Ti followed by CrN, and the TiN and CrN layers were deposited alternatively.

The X-ray reflectivity data of the coatings were recorded in a 2θ - ω geometry with a Philips X'pert PRO MPD (PW 3040/10) diffractometer. The X-ray source was a Cu K_α (0.15418 nm) radiation. The resolution of the goniometer was 0.001º. The reflectivity patterns were recorded in the range θ = 0 to 3º.

3. Results and discussion

3.1. Fitting procedure for specular X-ray reflection

Previous to the measurements, alignment of the sample stage has been performed for specular reflection by positioning the sample stage such that it half-cuts the direct X-ray beam in both ω and 2θ scans, independently. Due to the asymmetry in the sample shape, small values of offset in either ω or 2θ or both have been found and the same has been corrected in the software before performing the actual measurements. The simulation of the recorded patterns is carried out by employing X'Pert reflectivity program based on the Parrat formalism for specular X-ray reflection [21,37]. The Parrat formalism is based on successive reflection of low angle X-rays at many interfaces as in the case of a superlattice. The phase and amplitude of the reflected X-rays are functions of many parameters such as electron density, interface roughness, surface roughness and thickness. In order to begin with the simulation, we relied purely on the known experimental values which are either in the thin film or bulk form. For example, the electron density has been estimated from the mass density, which is available for the bulk materials. Experimental modulation wavelength has been calculated using Eq. 4. An absolute square root difference scheme has been used to minimize the difference between the experimental and the simulated results. The fitting has been tried with different procedures such as segmented fit,

genetic algorithm and a combination of both. It has been found that the fitting by segment method yielded the best results.

There are two main processes in the multilayer growth that cause the interface to broaden, namely, interdiffusion and intermixing. Intermixing is mixing of interfaces due to energetic particle bombardment, whereas, interdiffusion is thermally activated transport of material across the interface. Because of low substrate temperature (50-400°C) interdiffusion between TiN and CrN at the TiN/CrN and CrN/TiN interfaces has not been taken into consideration while simulating the data as the self-diffusion or interdiffusion of constituent elements/layers in transition metal nitrides is very low (e.g., $D_o = 4\times10^{-7}$ cm^2s^{-1} for N in TiN in the temperature range of 700-1400°C and $D_o = 7.0\times10^{-20}$ cm^2s^{-1} at T = 900°C for TiN/NbN superlattices) [38,39].

We have used a two layer model (i.e., without surface roughness layer) and a three layer model (i.e., with surface roughness layer) to fit with the experimental data. In the case of two layer model only the layers of TiN and CrN are considered in the simulation. But in the case of 3 layer model in addition to these two layers, one more layer on top of the superlattice has been considered, which one may define it either as a two layer with a roughness layer on top of it or a 3-layer. This is due to the fact that TiN when exposed to ambient forms an oxide layer of thickness 2-4 nm, because of preferential oxidation at the grain boundaries [40,41]. The best fits were obtained using a three layer model: (1) top surface roughness layer (approximately 1.7-3.6 nm), (2) TiN/CrN multilayer coating (approximately 1.8 μm) and (3) Ti interlayer (~0.5 μm) at the film-substrate interface. Similar additional oxide layers have been added on the top of various superlattice systems to fit the XRR data [27,32]. The schematic diagram of the three layer model is shown in figure. 1. The comparisons of experimental data with the two layer and

three layer models are shown in figures 2(a) and (b), which clearly show best fits for the three layer model. From the simulated XRR data, the mass densities of the TiN and CrN layers were calculated. Information on the thicknesses of the individual layers, electron densities, critical angle and the interface and surface roughnesses were also obtained from the simulated data.

3.2. Peak identification

The identification of the order of X-ray reflection peaks is a crucial step to calculate modulation wavelength using the modified Bragg's law. The peak identification is not a straight-forward process especially for nanolayered multilayer coatings. This is because some of the low-order peaks with a large modulation wavelength are embedded in the background or out of measurable incident angle range. So identification of the order of peaks is very important to calculate the modulation wavelength [42]. Yang and Zhao suggested a two-step approach to determine the order of reflection peaks [42]. First, an approximate Λ value is calculated from the peak angle interval ($\Delta 2\theta_{n+k,n}$):

$$\Delta 2\theta_{m+k,m} \approx \frac{180}{\pi} \cdot \frac{k\lambda}{\Lambda} = 57.3k \frac{\lambda}{\Lambda}, \qquad (5)$$

where k is the order of difference between the chosen peaks. The second step is to substitute the estimated Λ value into Eq. (4) in order to calculate the approximate positions of peaks with different orders by assuming $\delta = 10^{-5}$ and to determine the order of the reflection peaks in the XRR data. Based on this approach, we have assigned the order of peaks and calculated the modulation wavelength for TiN/CrN multilayer coatings. The possible error in calculating the modulation wavelength by this method is approximately 5%. The modulation wavelengths of the TiN/CrN multilayer coatings of the present study were calculated using modified Bragg's law. In the first plot, Λ was calculated from the slope of $\sin^2\theta_m$ vs. $(m\lambda)^2$. Typical plot of $\sin^2\theta_m$

vs. $(m\lambda)^2$ for the TiN/CrN multilayer coating is shown in figure 3(a). The slope ($4\Lambda^2$) of the curve was 3.774×10^{-16}. In the second graph, m^2 vs. $\sin^2\theta_m$ was plotted (figure 3(b)), which gives a straight line with a slope of $(\lambda/2\Lambda)^2$ and an intercept of 2δ. In this case, the slope of the line was 6.26791×10^{-5}. The δ value obtained from the second graph was 2.9412×10^{-5}. Modulation wavelengths of 9.71 and 9.72 nm were obtained from both the plots, as shown in figure 3. Similarly, the modulation wavelength was calculated for the other samples. As will be discussed later, the modulation wavelength calculated from the position of Bragg peaks (hereafter called estimated modulation wavelength) was in good agreement with the simulation results (hereafter called simulated modulation wavelength).

3.3. Effect of modulation wavelength on the interface properties

Typical X-ray reflectivity scans of approximately 1.8 μm thick TiN/CrN multilayer coatings at different modulation wavelengths are shown in figure 4. The substrate temperature was 400 ºC and the substrate bias was -200 V for these samples. Values of various parameters obtained from the reflectivity data fitted by the theoretical simulation at different modulation wavelengths are presented in Table 2. The estimated modulation wavelength values are close to the simulated modulation wavelength values, which are shown in figure 5(a). At Λ = 6.6 and 12.8 nm, only reflections of 3rd orders could be seen. Maximum order of reflections up to 5th order were observed for Λ = 9.7 nm, which is more clearly shown in the inset of figure 4, wherein we have plotted θ vs. $I\theta^4$. It is known that for angle of incidence higher than θ_c, the reflectivity drops with increasing angle θ as θ^4 [43]. As the coating thickness is high (~1.8 μm), no Kiessig's fringes were observed due to the instrumental limitation and high absorption coefficients of the component materials [44,45].

The intensity ratio of the first and second order Bragg peaks (I_1/I_2) as a function of modulation wavelength is shown in figure 5(b). As the modulation wavelength increases, the intensity ratio of the first order and second order Bragg peaks decreases. It is known that the higher order Bragg peaks are roughness sensitive, therefore, the decrease in the intensity ratio of first and second order Bragg peaks indicates an increase in the roughness [32]. The roughness depends upon (i) the number of bilayers, (ii) the bilayer thickness and (iii) the ratio of individual layer thicknesses [46]. The intensity of the XRR peaks is reported to reduce by a Debye-Waller like factor exp ($-2k_1k_2\sigma^2$), where k_1 and k_2 are wave vectors in the constituent layers and σ is the interface roughness [27]. Theoretically, it has been shown that for Cr/Sc multilayers a decrease in the interface roughness from 0.5 to 0.3 nm in a multilayer with a modulation wavelength 1.692 nm corresponds to an increase in normal-incidence reflectivity from 2-19% [32]. There are other causes for reduction in the intensity of XRR peaks. These include: long-range waviness of the sample beyond the limits of resolution of the diffractometer and surface roughness [32].

It is found that as Λ increases from 4.6 to 9.7 nm, intensity of the reflected beam, just below the critical angle, decreases from its maximum value at 4.6 nm. On further increasing Λ, the intensity of the reflected beam increases from its minimum value at 9.7 nm. Furthermore, at Λ = 12.8 nm, the first Bragg peak has a low scattering vector ($q = 4\pi\sin\theta/\lambda$) value (0.0068 nm^{-1}) and is very close to q_c (0.0049 nm^{-1}), so it is difficult to resolve the first order Bragg peak, as shown in figure 4. As the modulation wavelength decreases, the first Bragg peak shifts towards higher q and becomes clearly resolved (for example, for Λ = 4.6 nm, q = 0.01441 nm^{-1} and q_c = 0.0052 nm^{-1}) [30].

The electron density of the TiN and CrN layers can be calculated from their mass density values [28]:

$$\rho_e = \rho N_A \frac{\sum_i (Z_i + f_i)}{\sum_i M_i}. \quad (6)$$

where ρ is the mass density, N_A is the Avogadro constant, Z_i is the atomic number of the i^{th} element and M_i is the atomic weight. The parameter f is defined as:

$$f = Z_i + f_i^{'} + if_i^{''}, \quad (7)$$

where $f_i^{'}$ and $f_i^{''}$ are real and imaginary anomalous dispersion factors, respectively.

The mass densities of TiN and CrN layers prepared at various modulation wavelengths were found to be in the ranges of 4.149 – 4.895 and 4.240 – 5.080 g/cm^3, respectively, which are shown in Table 2. The simulated mass densities for TiN and CrN layers are lower than the corresponding bulk densities (5.210 and 6.10 g/cm^3 for TiN and CrN, respectively). This may be attributed to the columnar structure of TiN/CrN multilayers and incorporation of Ar in the film (approximately 2-3 at.%). Argon was believed to be incorporated during the deposition (*in situ* Ar^+ ion bombardment of the growing film). The presence of columnar grains is a common feature in lattice mismatched films considering 2.5% mismatch between TiN and CrN [47]. The columnar structure allows pores or voids existing between the columns to grow and thus lowers the value of density. It has been shown that the porosity of PVD coatings increases significantly at low thicknesses [48]. The electron density of bulk TiN (1481 e^-/nm^3) was calculated from the bulk mass density value. The electron density of TiN layer (1179-1468 e^-/nm^3) is lower than the bulk electron density. This deviation in the electron density of TiN from the bulk value is believed to be due to the formation of columnar/porous microstructure of TiN layer. The electron density of CrN also shows a similar trend.

It is evident from the Table 2, the roughness of CrN layer was always higher than that of TiN layer and is attributed to higher growth rate of CrN (0.6 nm/s) as compared to TiN layer (0.2 nm/s) [49]. Higher partial pressure of N_2 near the Cr target, as discussed in the Experimental Section, is also believed to be responsible for higher roughness of CrN layer [27]. In general, for multilayer coatings prepared with a bilayer thickness of 4.6-9.7 nm, no significant change in the surface roughness was observed. However, multilayer coatings prepared at higher modulation wavelength (12.8 nm) exhibited relatively high surface roughness, suggesting that modulation wavelength plays an important role in controlling the surface roughness of TiN/CrN superlattices [50]. For thin films (that is single layer), theoretically, it has been shown that the width of the interface (σ) scales with thickness (t) by the general relation $\sigma \approx t^{\beta}$ with β = 0.2-0.5. Furthermore, for the sputtered films the substrate temperature is low compared to the melting temperature of deposited materials (2950 ºC for TiN and 1500 ºC for CrN), the expected surface morphology consists of columns, with a characteristic length ξ which scales with thickness as $\xi \approx t^{p}$ with p as the scaling exponent [27]. For multilayer film, however, the roughness evolution is more complex because of existence of many buried interfaces [49]. Decrease in the surface roughness at low modulation wavelength has been attributed to interruption of columnar grains because of alternating deposition of constituent layers [51]. Our results are in good agreement with those reported in the literature [50,52].

At Λ = 9.7 nm, maximum order of reflections up to 5th order were observed at θ_1 = 0.58 deg., θ_2 = 0.94 deg., θ_3 = 1.39 deg., θ_4 = 1.85 deg. and θ_5 = 2.30 deg. The difference in the positions of successive Bragg reflections was approximately constant ($\Delta\theta \sim$ 0.45 deg.). The maximum order of reflections and the uniform spacing between the Bragg reflections, indicate well-defined periodicity along the growth direction and relatively sharp interfaces [53].

However, the order of reflections and their intensities were very low at Λ = 12.8 nm, because of its high surface (3.682 nm) and interface roughnesses (0.891 and 1.072 nm, respectively for TiN and CrN layers).

At Λ = 12.8 nm, significant broadening of higher order peaks was also observed, indicating that small layer thickness fluctuations may be present [53,54]. The thickness fluctuations (discrete and continuous) give rise to cumulative disorder and destroy the long-range order of the superlattice, resulting in main Bragg peak broadening as well as in dampening of higher order Bragg peak intensities [30,53].

3.4. Effect of substrate temperature on the interface properties

Figure 6 shows the XRR patterns of TiN/CrN multilayer coatings deposited at different substrate temperatures in the range 50 – 400 ºC. The nominal modulation wavelength was 9.0 nm and the substrate bias was -200 V for these samples. At T_s = 50, 200 and 300 ºC, reflection peaks up to 4^{th} order were observed and the maximum order of reflections (5^{th} order) were observed for coating deposited at 400 ºC. This indicates the well-defined periodicity of the constituent layers along the growth direction and the presence of relatively sharp interfaces for coatings prepared at substrate temperature of 400 ºC. This has been further confirmed from the simulation results presented in Table 3. The interface roughness of TiN did not change significantly with the substrate temperature, however with an increase in the substrate temperature σ_{CrN} decreased significantly. Similarly, the surface roughness decreased with increasing substrate temperature. It has been reported that low substrate temperature during growth minimizes interdiffusion and intermixing. Such conditions may lead to kinematically limited growth, i.e., the adatoms do not have high enough surface mobility to find the energetically most favorable sticking position. This leads to increased and accumulated

roughness [32]. At 400 ºC, we observed a shift in the position of Bragg peaks towards lower θ values. The shift in the peak is due to an increase in the modulation wavelength at 400 ºC, the exact reason for this is not clearly known.

3.5. Effect of substrate bias on the interface properties

The XRR patterns of TiN/CrN multilayer coatings deposited at different substrate bias voltages in the range -50 to -200 V are shown in figure 7. The nominal modulation wavelength was 9.0 nm and the substrate temperature was 400ºC for these samples. At V_B = -50 V, no Bragg reflections were observed and further increase in the bias voltage resulted in the appearance of Bragg reflections. As the bias voltage increases beyond -50 V, the order of the Bragg reflections also increased. It is evident from figure 7 and the simulated data given in Table 4 that the coating deposited at V_B = -50 V has high surface (3.500 nm) and interface roughnesses (1.169 and 1.721 nm for TiN and CrN layers, respectively). It has been reported that at low ion energies, i.e., for low mobility of the adatoms, the kinematically limited growth will produce asperities, with relatively loosely bound top atoms, on the surface. This leads to an increased and accumulated roughness as the growth of the multilayer proceeds [32]. Due to this, the radiation reflected from the surface does not interfere constructively with the radiation reflected from the interface, causing the disappearance of reflection peaks [55]. At V_B = -200 V, maximum order of reflections (5^{th} order) were observed, indicating a well-defined periodicity of the constituent layers. Also at this substrate bias, low surface (2.044 nm) and interface roughness values (0.577 and 0.918 nm for TiN and CrN layers, respectively) were observed, indicating the presence of sharp interfaces. This is because, as the ion energy increases, the loosely bound atoms will move around on the surface and find positions where they minimize the total energy, which results in smooth surface morphology [32].

The foregoing discussion indicated that TiN/CrN superlattices prepared at a modulation wavelength of 9.7 nm, a substrate bias of -200 V and a substrate temperature of 400°C exhibited well-defined periodicity of the constituent layers, relatively sharp interfaces and low surface and interface roughnesses. The coatings prepared at a modulation wavelength of 9.7 nm, a substrate bias of -200 V and a substrate temperature of 400°C also exhibited superior mechanical properties [3]. Therefore, the simulation results are consistent with the mechanical properties of the TiN/CrN superlattices. The effect of substrate temperature, substrate bias and modulation wavelength onto the growth of TiN/CrN superlattices is briefly discussed below.

For practical applications, any multilayer hard coating should fulfill complex requirements such as hardness, toughness and good adherence at the substrate-coating interface. The properties of multilayered coatings are determined by the microstructure (density, grain size, grain boundaries, grain orientation) and sharp interfaces, which are critically affected by the deposition parameters such as bilayer thickness, substrate temperature and substrate bias. For sputter deposited coating, generally the growth temperature (T/T_m, where T_m is the melting temperature of the material) is less than or equal to 0.3. This is commonly known as Zone 1 of the Thornton model of thin film growth [50]. The zone is characterized by a columnar fine grain microstructure. A substrate temperature of 200 - 400 ºC is ideal for practical applications such as deposition on metallic substrates, leading to good adhesion between the substrate and the coating. Similarly, considerable amount of ion bombardment is required to increase the hardness of the coating. In the present case, the ion current densities were 1.1 and 0.3 mA/cm^2 for TiN and CrN layers, respectively at a substrate bias of -200 V. It has been reported that for a substrate bias of -150 to -200 V, the ion bombardment results in ion induced densification, whereas at higher substrate bias voltages, deterioration in the multilayer structure is caused by

interdiffusion and interface roughness [56]. The ion bombardment during the film growth suppresses the formation of large grains with voided or cracked boundaries because of continuous renucleation process. Increasing the substrate bias increases the energy of impinging ions and as a result re-sputtering occurs. Furthermore, as the energy of the impinging ions increases, the generation of defects and preferential re-sputtering of adatoms increase, these processes in turn produce an increased number of preferential nucleation sites which reduce the grain size. The ion bombardment also results in trapping of accelerated gas ions (e.g., Ar and N_2) and high compressive stresses in the coating [57].

An optimum bilayer thickness is required to have high hardness of the multilayer coating because at moderate bilayer thicknesses, the thicknesses of the component layers are small and dislocation generation mechanism such as Frank-Read sources cannot operate inside a given layer [58]. Furthermore, even dislocations are generated in the layers, they propagate towards the interfaces. As the interfacial energies are quite high, further movement of the dislocations is prevented and hence pile up of dislocations takes place near the interfaces [58,59], resulting in enhanced hardness of multilayer coatings. At very low bilayer thicknesses, however the interfaces are not sharp resulting in a decrease in the hardness of multilayer coatings. Therefore, a judicious control of various process parameters is required to obtain best quality multilayer coatings.

4. Conclusions

X-ray reflectivity was used to determine the interface roughness, surface roughness, electron density, critical angle and modulation wavelength of TiN/CrN superlattices deposited at various process conditions. A modified Bragg's law was used to calculate the modulation wavelength from the experimentally observed XRR data. Bragg reflections up to 5^{th} order were

observed for TiN/CrN superlattice coatings prepared at a modulation wavelength of 9.7 nm, a substrate bias of -200 V and a substrate temperature of 400ºC, indicating well-defined periodicity of the constituent layers and smooth interfaces. The experimentally obtained XRR data were simulated using theoretically generated data by applying a three layer model. Simulation showed that the superlattice coatings prepared under the above conditions exhibited a surface roughness of 2.044 nm and interface roughnesses of 0.577 and 0.918 nm for TiN and CrN layers, respectively. The roughness of CrN layer was always higher than that of TiN layer and is attributed to higher growth rate of CrN as compared to TiN layer and high partial pressure of nitrogen near the Cr target. Multilayer coatings prepared at high modulation wavelength (12.8 nm) exhibited relatively high surface roughness. Decrease in the surface roughness at low modulation wavelength has been attributed to interruption of columnar grains because of alternating deposition of constituent layers. Furthermore, simulated modulation wavelength values were in agreement with the modulation wavelengths calculated from the modified Bragg's law. The electron densities of the individual layers were calculated from the simulated mass densities. Both the mass and electron densities were less than that of the bulk values, indicating porous/columnar microstructure of TiN and CrN layers. A decrease in the intensity ratio of first and second order Bragg peaks with modulation wavelength was observed, which has been attributed to an increase in the roughness. Detailed investigations showed that the substrate temperature and the substrate bias critically affected the interface and surface roughnesses of TiN/CrN multilayers.

ACKNOWLEDGEMENTS

We thank Director, NAL, Council of Scientific and Industrial Research (CSIR), New Delhi for giving permission to publish these results. Kanwal Preet Bhatti is thanked for XRR

measurements. This work was supported by CSIR Networked Projects on “Developing and Sustaining High Science Technology for National Aerospace Programs” under the Project No. I-888-1/37.

References

[1] Yashar P, Barnett S A, Rechner J and Sproul W D 1998 *J. Vac. Sci. Technol. A* **16** 2913

[2] Nordin M, Larsson M and Hogmark S 1998 *Surf. Coat. Technol.* **106** 234

[3] Barshilia H C, Jain A and Rajam K S 2004 *Vacuum* **72** 241

[4] Barshilia H C and Rajam K S 2004 *Surf. Coat. Technol.* **183** 174

[5] Barshilia H C, Prakash M S, Poojari A and Rajam K S 2004 *Thin Solid Films* **460** 133

[6] Barshilia H C, Prakash M S, Jain A and Rajam K S 2005 *Vacuum* **77** 169

[7] Barshilia H C and Rajam K S 2004 *J. Mater. Res.* **19** 3196

[8] Logothetidis S, Kalfagiannis N, Sarakinos K and Patsalas P 2006 *Surf. Coat. Technol.* **200** 6176.

[9] Soe W H and Yamamoto R 1997 *Mater. Chem. Phys.* **50** 176

[10] Cavaleiro A and De Hosson Jeff Th M 2006 *Nanostructured Coatings* (New York: Springer)

[11] Lin C S, Ke C S and Peng H 2001 *Surf. Coat. Technol.* **146-147** 168

[12] Nordin M, Herranen M and Hogmark S 1999 *Thin Solid Films* **348** 202

[13] Yang Q, He C, Zhao L R and Immarigeon J P 2002 *Scripta Materialia* **46** 293

[14] Nordin M, Larsson M and Hogmark S 1999 *Wear* **232** 221

[15] Panjan P, Navinsek B, Cvelbar A, Zalar A and Vlcek J 1998 *Surf. Coat. Technol.* **98** 1497

[16] Panjan P, Navinsek B, Cvelbar A, Zalar A and Milosev I 1996 *Thin Solid Films* **281-282** 298

[17] Zeng X T, Zhang S, Sun C Q and Liu Y C 2003 *Thin Solid Films* **424** 99

[18] Sugawara M, Kondo M, Yamazaki S and Nakajima K 1988 *Appl. Phys. Lett.* **52** 742

[19] Payne A P and Clemens B M 1993 *Phys. Rev. B* **47** 2289

[20] Barshilia H C, Rajam K S and Rao D V S 2006 *Surf. Coat. Technol.* **200** 4586

[21] Parratt L G 1954 *Phys. Rev.* **95** 359

[22] Brown J C 1966 *X-rays and Their Applications* (New York: Plenum Press)

[23] Yashar P C and Sproul W D 1999 *Vacuum* **55** 179

[24] Yang Q and Zhao L R 2005 *Surf. Coat. Technol.* **200** 1709

[25] Miceli P F, Neumann D A and Zabel H 1986 *Appl. Phys. Lett.* **48** 24

[26] Ferrari A C, Libassi A, Tanner B K, Stolojan V, Yuan J, Brown L M, Rodil S E, Kleinsorge B and Robertson J 2000 *Phys. Rev. B* **62** 11089

[27] Fullerton E E, Pearson J, Sowers C H, Bader S D, Wu X Z and Sinha S K 1993 *Phys. Rev. B* **48** 17432

[28] Birkholz M, Fewster P F and Genzel C 2006 *Thin Film Analysis by X-ray Scattering* (New York: Wiley-VCH)

[29] Aldareguia J M M 2002 *Ph.D. Thesis*, University of Cambridge, 2002

[30] Huai Y, Cochrane R W and Sutton M 1993 *Phys. Rev. B* **48** 2568

[31] Bernabe A de, Capitan M J, Fischer H E, Quiros C, Prieto C, Colino J, Mompean F and Sanz J M 1999 *Surf. Interface Anal.* **27** 1.

[32] Eriksson F, Johansson G A, Hertz H M and Birch J 2002 *Opt. Eng.***41** 2903

[33] Ulyanenkov A, Matsuo R, Omote K, Inaba K, Harada J, Ishino M, Nishii M and Yoda O J 2000 *Appl. Phys.***87** 7255

[34] Liu Z J, Vyas A, Lu Y H and Shen Y G 2005 *Thin Solid Films* **479** 31

[35] Weast R C and Astle M J 1982 *CRC Hand Book of Chemistry and Physics* (Florida: CRC Press Inc)

[36] Toth L E 1971 *Transition Metal Carbides and Nitrides* (New York: Academic Press)

[37] Philips X'PERT PRO Manual Number PW 3040.

[38] Hultman L, Engstrom C and Oden M 2000 *Surf. Coat. Technol.* **133-134** 227

[39] Hultman L 2000 *Vacuum* **57** 1

[40] Franck M, Celis J P and Roos J R 1995 *J. Mater. Res.* **10** 119

[41] Ernsberger C, Nickerson J, Smith T, Miller A E and Banks D 1986 *J. Vac. Sci. Technol. A.* **4** 2784

[42] Yang Q and Zhao L R Mater. Character. (in press)

[43] Bauer G and Richter W 1996 *Optical Characterization of Epitaxial Semiconductor Layers*, (Berlin-Heidelberg: Springer-Verlag)

[44] Abadias G, Tse Y Y, Guerin P h and Pelosin V J 2006 *Appl. Phys.* **99** 113519

[45] Aschentrup A, Hachmann W, Westerwalbesloh T, Lim Y C, Kleineberg U and Heinzmann U 2003 *Appl. Phys. A.* **77** 607

[46] Paul A and Lodha G S 2002 *Phys. Rev. B* **65** 245416

[47] Mirkarimi P B, Barnett S A, Hubbard K M, Jervis T R and Hultman L 1994 *J. Mater. Res.* **9** 1456

[48] Jehn H A 2000 *Surf. Coat. Technol.***125** 212

[49] Liu Z J and Shen Y G 2004 *Appl. Phys. Lett.***84** 5121

[50] Savage D E, Schimke N, Phang Y H and Lagally M G 1992 *J. Appl. Phys.* **71** 3283

[51] Wang X, Kolitsch A and Moller W 1997 *Appl. Phys. Lett.***71** 1951

[52] Walton C C, Thomas G and Kortright J B 1998 Acta Mater. **46** 3767

[53] Lamelas F J, He H D and Clarke R 1991 *Phys. Rev. B* **43** 12296

[54] Clemens B M and Gay J G 1987 *Phys. Rev. B* **35** 9337

[55] Santucci S, Giuliani P, Picozzi P, Phani A R, Biase M D, Alfonsetti R, Moccia G and Missori M 2000 *Thin Solid Films* **360** 89.

[56] Helmersson U, Todorova S, Barnett S A, Sundgren J E, Markert L C, Greene J E. 1987 *J. Appl. Phys.* **62** 481.

[57] Perry A J 1990 *J. Vac. Sci. Technol. A* **8** 1351

[58] Koehler J S 1970 *Phys. Rev. B* **2** 547

[59] Foecke T and Lashmore D S 1992 *Scripta Met. Mater.* **27** 651

Figure Captions

Figure 1. Schematic diagram of the three layer model used for the X-ray reflectivity simulations.

Figure 2. Comparison of the experimental XRR data with (a) two layer and (b) three layer models. The dotted curves represent the simulated data.

Figure 3. Calculation of modulation wavelength using modified Bragg's law: (a) Plot of $\sin^2\theta_m$ vs. $(m\lambda)^2$ and (b) Plot of m^2 vs. $\sin^2\theta_m$. See text for details.

Figure 4. Experimental and simulated low angle X-ray reflectivity patterns of TiN/CrN multilayer coatings deposited at various modulation wavelengths. Also shown is a plot of θ vs. $I\theta^4$ for the multilayer with a modulation wavelength of 9.7 nm.

Figure 5. (a) Plot of modulation wavelength of TiN/CrN multilayer coatings determined from Bragg peak positions and simulation data and (b) Plot of intensity ratio of first and second order Bragg reflections with modulation wavelength.

Figure 6. Low angle X-ray reflectivity patterns of TiN/CrN multilayer coatings deposited at various substrate temperatures. Also shown are the theoretically generated XRR patterns.

Figure 7. Low angle X-ray reflectivity patterns of TiN/CrN multilayer coatings deposited at different substrate bias voltages. Also shown are the theoretically generated XRR patterns.

Table 1. Process parameters for the deposition of TiN/CrN multilayers deposited at various modulation wavelengths.

Sample No.	**Nominal Modulation Wavelength (nm)**	**Substrate Temperature (ºC)**	**Substrate Bias (V)**	**No. of Bilayers**
1	4.0	400	-200	417
2	6.0	400	-200	277
3	9.0	400	-200	208
4	12.0	400	-200	128

Table 2. Values of the parameters obtained from the X-ray reflectivity data fitted by the theoretical simulation for the TiN/CrN superlattices prepared at different modulation wavelengths. σ_{TiN} is defined as roughness of TiN on CrN and σ_{CrN} is defined as roughness of CrN on TiN.

Nominal Modulation Wavelength (nm)	**Estimated Modulation Wavelength (nm)**	**Simulated Modulation Wavelength (nm)**	**Critical Angle (deg.)**	**Electron Density (e^- nm^{-3})**		**Fitted Thickness (nm)**		**Fitted Density (g/cm^3)**		**Fitted Roughness (nm)**		
				TiN	**CrN**	t_{TiN}	t_{CrN}	ρ_{TiN}	ρ_{CrN}	σ_{TiN}	σ_{CrN}	σ_o
4.0	4.6	4.631	0.368	1391	1429	2.409	2.222	4.895	5.080	0.698	1.32	2.547
6.0	6.6	6.693	0.345	1179	1129	3.688	3.005	4.149	4.240	0.632	1.006	2.420
9.0	9.7	9.689	0.368	1468	1380	5.905	3.784	4.727	4.906	0.577	0.918	2.044
12.0	12.8	12.89	0.351	1296	1275	7.483	5.407	4.561	4.534	0.891	1.072	3.682

Table 3. Values of the parameters obtained from the X-ray reflectivity data fitted by the theoretical simulation for the TiN/CrN superlattices prepared at different substrate temperatures.

Substrate Temp. (°C)	***Estimated Modulation Wavelength (nm)**	**Simulated Modulation Wavelength (nm)**	**Critical Angle (deg.)**	**Electron Density ($e^- nm^{-3}$)**		**Fitted Thickness (nm)**		**Fitted Density (g/cm^3)**		**Fitted Roughness (nm)**		
				TiN	**CrN**	t_{TiN}	t_{CrN}	ρ_{TiN}	ρ_{CrN}	σ_{TiN}	σ_{CrN}	σ_o
50	8.2	8.227	0.331	1413	1468	5.255	2.972	4.971	5.220	0.528	1.441	2.624
200	7.9	7.917	0.290	1443	1510	5.151	2.766	5.078	5.369	0.560	1.381	2.389
300	7.6	7.661	0.322	1437	1439	4.262	3.399	5.056	5.307	0.699	1.344	2.200
400	9.7	9.689	0.368	1468	1380	5.905	3.784	4.727	4.906	0.577	0.918	2.044

* The nominal modulation wavelength was 9.0 nm

Table 4. Values of the parameters obtained from the X-ray reflectivity data fitted by the theoretical simulation for the TiN/CrN superlattices prepared at different substrate bias voltages.

Substrate Bias (V)	***Estimated Modulation Wavelength (nm)**	**Simulated Modulation Wavelength (nm)**	**Critical Angle (deg.)**	**Electron Density ($e^- nm^{-3}$)**		**Fitted Thickness (nm)**		**Fitted Density (g/cm^3)**		**Fitted Roughness (nm)**		
				TiN	**CrN**	t_{TiN}	t_{CrN}	ρ_{TiN}	ρ_{CrN}	σ_{TiN}	σ_{CrN}	σ_o
-50	9.8	9.892	--	1224	1250	4.960	4.932	4.307	4.399	1.169	1.721	3.500
-100	9.3	9.356	0.303	1439	1463	4.729	4.627	5.063	5.148	0.593	1.365	1.791
-200	9.7	9.689	0.368	1468	1380	5.905	3.784	4.727	4.906	0.577	0.918	2.044

* The nominal modulation wavelength was 9.0 nm.

Fig. 1

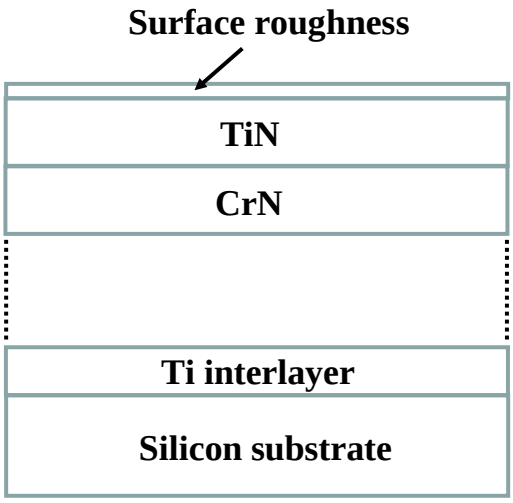
Surface roughness
TiN
CrN
Ti interlayer
Silicon substrate

Fig. 2

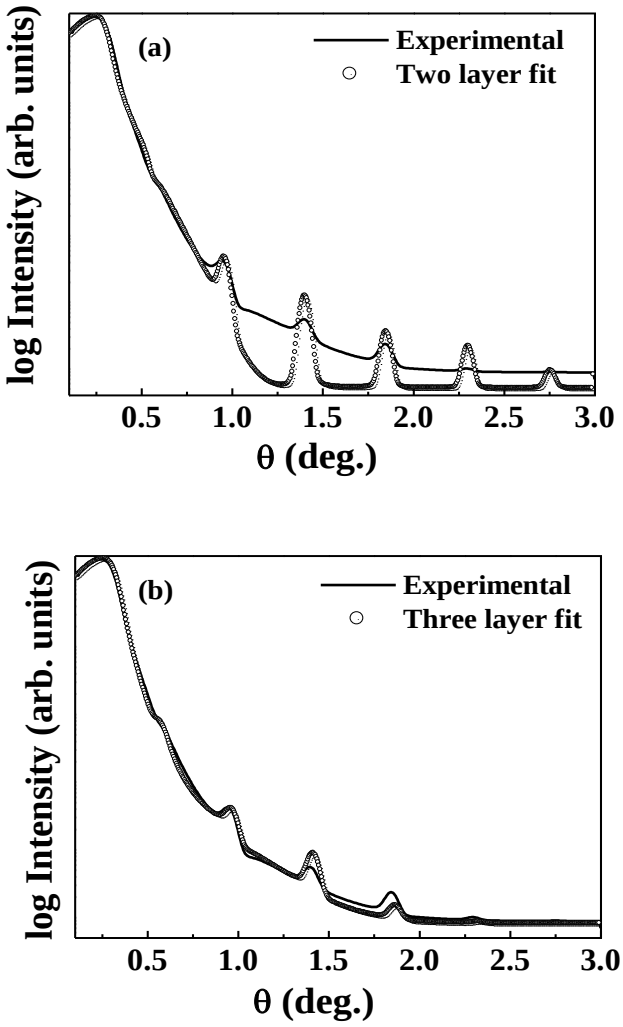
(a)
Experimental
Two layer fit
log Intensity (arb. units)
0.5
1.0
1.5
2.0
2.5
3.0
θ (deg.)
(b)
Experimental
Three layer fit
log Intensity (arb. units)
0.5
1.0
1.5
2.0
2.5
3.0
θ (deg.)

Fig. 3

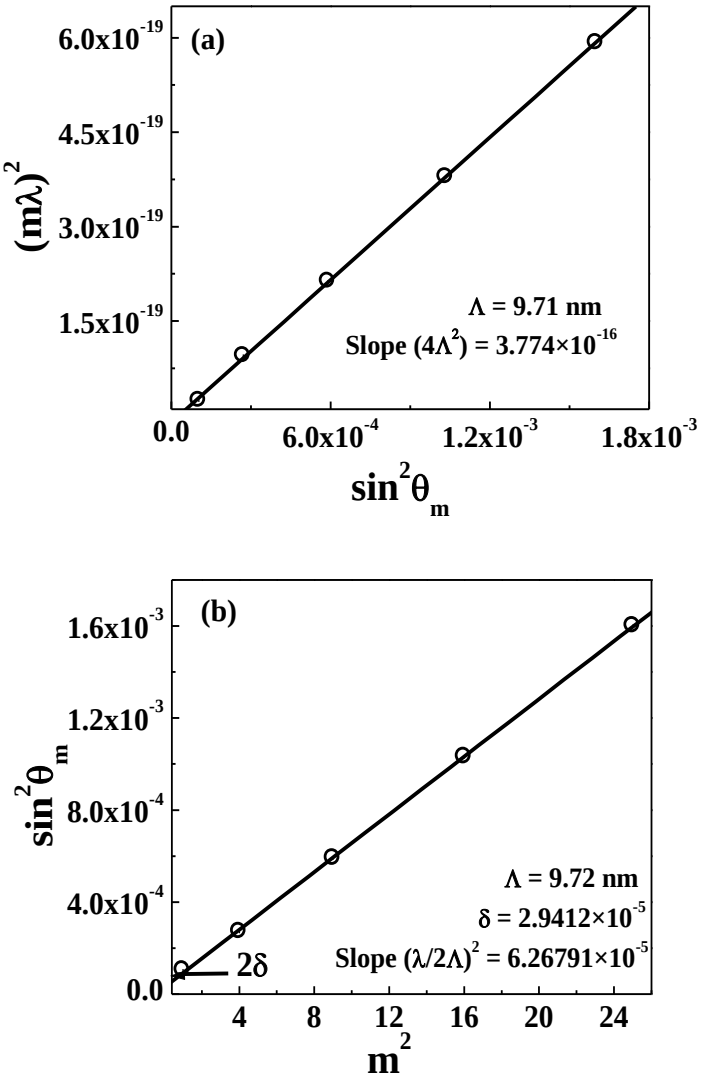
(a)
6.0x10^-19
4.5x10^-19
3.0x10^-19
1.5x10^-19
(mλ)^2
Λ = 9.71 nm
Slope (4Λ^2) = 3.774×10^-16
0.0
6.0x10^-4
1.2x10^-3
1.8x10^-3
sin^2θ_m
(b)
1.6x10^-3
1.2x10^-3
8.0x10^-4
4.0x10^-4
0.0
sin^2θ_m
Λ = 9.72 nm
δ = 2.9412×10^-5
Slope (λ/2Λ)^2 = 6.26791×10^-5
2δ
4
8
12
16
20
24
m^2

Fig. 4

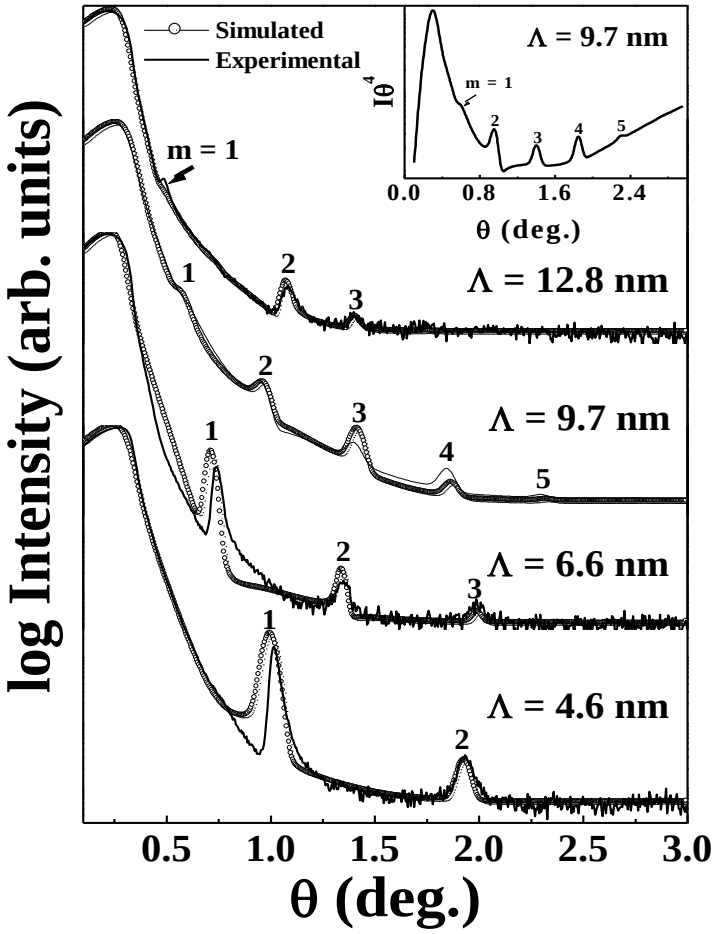
Simulated
Experimental
Λ = 9.7 nm
Iθ^4
m = 1
2
3
4
5
0.0
0.8
1.6
2.4
θ (deg.)
m = 1
1
2
3
Λ = 12.8 nm
2
3
1
4
5
Λ = 9.7 nm
2
3
1
Λ = 6.6 nm
1
2
Λ = 4.6 nm
log Intensity (arb. units)
0.5
1.0
1.5
2.0
2.5
3.0
θ (deg.)

Fig. 5

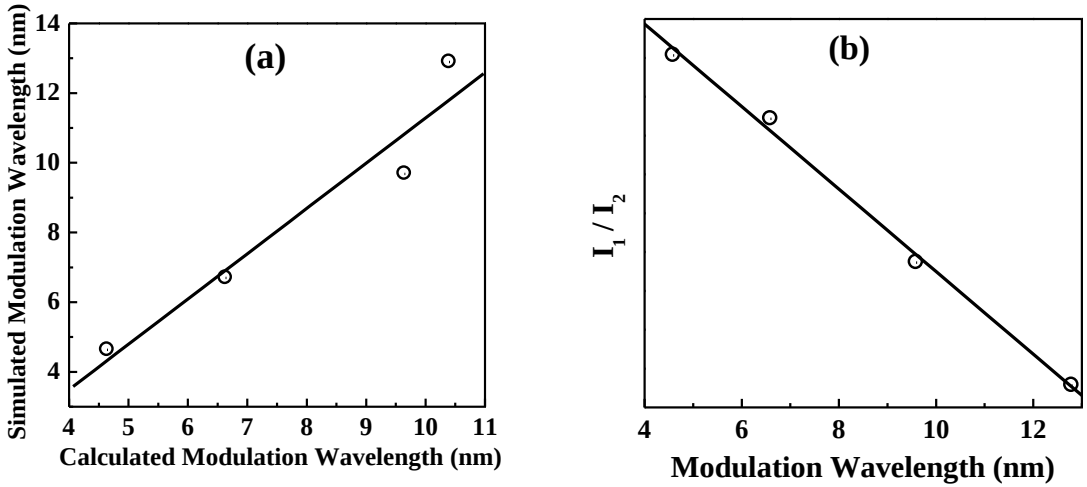
(a)
Simulated Modulation Wavelength (nm)
Calculated Modulation Wavelength (nm)
4
5
6
7
8
9
10
11
4
6
8
10
12
14
(b)
I_1 / I_2
Modulation Wavelength (nm)
4
6
8
10
12

Fig. 6

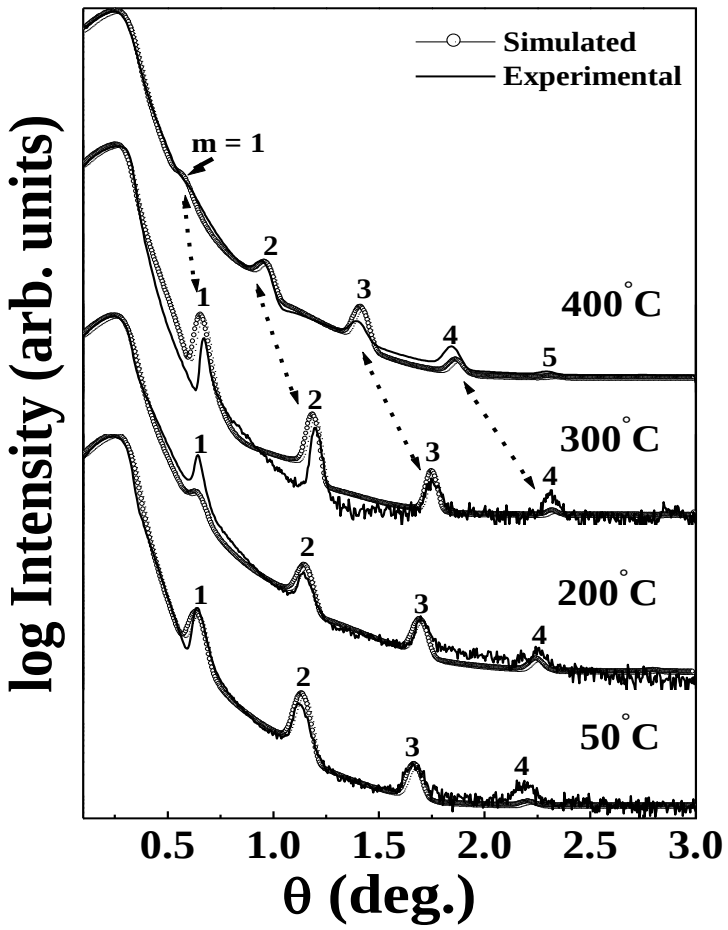
Simulated
Experimental
m = 1
400°C
300°C
200°C
50°C
log Intensity (arb. units)
θ (deg.)
0.5
1.0
1.5
2.0
2.5
3.0

Fig. 7

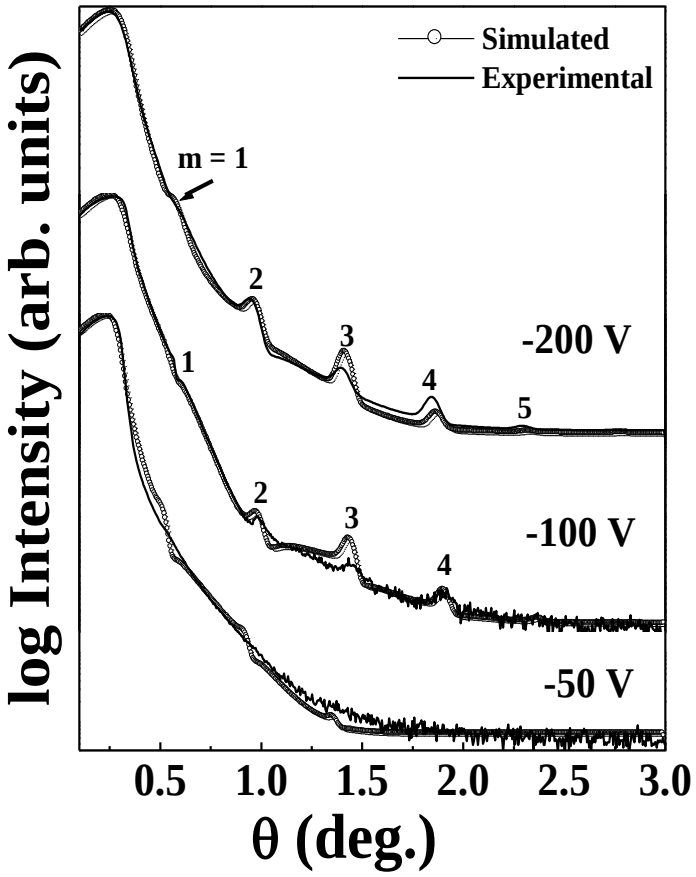
Simulated
Experimental
m = 1
2
3
4
5
-200 V
1
2
3
4
-100 V
-50 V
log Intensity (arb. units)
0.5
1.0
1.5
2.0
2.5
3.0
θ (deg.)